



Since January 2020 Elsevier has created a COVID-19 resource centre with free information in English and Mandarin on the novel coronavirus COVID-19. The COVID-19 resource centre is hosted on Elsevier Connect, the company's public news and information website.

Elsevier hereby grants permission to make all its COVID-19-related research that is available on the COVID-19 resource centre - including this research content - immediately available in PubMed Central and other publicly funded repositories, such as the WHO COVID database with rights for unrestricted research re-use and analyses in any form or by any means with acknowledgement of the original source. These permissions are granted for free by Elsevier for as long as the COVID-19 resource centre remains active.



Rapid determination of SARS-CoV-2 nucleocapsid proteins based on 2D/2D MXene/P-BiOCl/Ru(bpy)₃²⁺ heterojunction composites to enhance electrochemiluminescence performance

Xuebo Liu^a, Liwei Bai^a, Xiaowei Cao^b, Feng Wu^c, Tao Yin^d, Wenbo Lu^{a,*}

^a Key Laboratory of Magnetic Molecules and Magnetic Information Materials (Ministry of Education), School of Chemistry and Material Science, Shanxi Normal University, Taiyuan, 030031, China

^b Institute of Translational Medicine, Medical College, Yangzhou University, Yangzhou, 225001, China

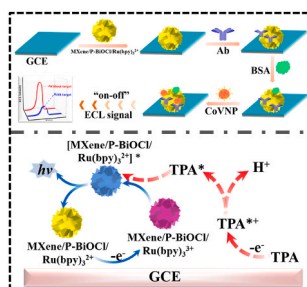
^c School of Medicine, Jiangsu University, Zhenjiang, 212013, China

^d College of Medical Imaging, Shanxi Medical University, Taiyuan, 030001, China

HIGHLIGHTS

- Two-dimensional (2D) material ultrathin P-BiOCl is exploited and first applied in ECL.
- 2D architectures MXene act as “soft substrate” to improve the properties of P-BiOCl and synergistically work with P-BiOCl.
- MXene/P-BiOCl/Ru(bpy)₃²⁺ is an efficient signal amplifier and co-reaction accelerator in the presence of TPA as a coreactant.
- A “signal on-off” ECL biosensor MXene/P-BiOCl/Ru(bpy)₃²⁺/GCE can specifically recognize SARS-CoV-2 nucleocapsid protein.

GRAPHICAL ABSTRACT



ARTICLE INFO

Keywords:

SARS-CoV-2 nucleocapsid protein
MXene/P-BiOCl/Ru(bpy)₃²⁺
Electrochemiluminescence
“Signal on-off” ECL immunosensors
Signal amplifier and co-reaction accelerator

ABSTRACT

At the end of 2019, the novel coronavirus disease 2019 (COVID-19), a cluster of atypical pneumonia caused by the severe acute respiratory syndrome coronavirus 2 (SARS-CoV-2), has been known as a highly contagious disease. Herein, we report the MXene/P-BiOCl/Ru(bpy)₃²⁺ heterojunction composite to construct an electrochemiluminescence (ECL) immunosensor for SARS-CoV-2 nucleocapsid protein (CoVNP) determination. Two-dimensional (2D) material ultrathin phosphorus-doped bismuth oxychloride (P-BiOCl) is exploited and first applied in ECL. 2D architectures MXene not only act as “soft substrate” to improve the properties of P-BiOCl, but also synergistically work with P-BiOCl. Owing to the inimitable set of bulk and interfacial properties, intrinsic high electrochemical conductivity, hydrophilicity and good biocompatible of 2D/2D MXene/P-BiOCl/Ru(bpy)₃²⁺, this as-exploited heterojunction composite is an efficient signal amplifier and co-reaction accelerator in the presence of tri-n-propylamine (TPA) as a coreactant. The proposed MXene/P-BiOCl/Ru(bpy)₃²⁺-TPA system exhibits a high and stable ECL signal and achieves ECL emission quenching for “signal on-off” recognition of CoVNP. Fascinatingly, the constructed ECL biosensor towards CoVNP allows a wide linear concentration range from 1 fg/mL to 10 ng/mL and a low limit of detection (LOD) of 0.49 fg/mL (S/N = 3). Furthermore, this presented strategy sheds light on designing a highly efficient ECL nanostructure through the combination of 2D

* Corresponding author.

E-mail address: luwb@sxnu.edu.cn (W. Lu).

<https://doi.org/10.1016/j.aca.2022.340522>

Received 7 August 2022; Received in revised form 29 September 2022; Accepted 12 October 2022

Available online 17 October 2022

0003-2670/© 2022 Elsevier B.V. All rights reserved.

MXene architectures with 2D semiconductor materials in the field of nanomedicine. This ECL biosensor can successfully detect CoVNP in human serum, which can promote the prosperity and development of diagnostic methods of SARS-CoV-2.

1. Introduction

The novel coronavirus disease 2019 (COVID-19), a cluster of atypical pneumonia caused by the severe acute respiratory syndrome coronavirus 2 (SARS-CoV-2), has been known as a highly contagious disease. Owing to the rapid spread and multiple routes of transmission of SARS-CoV-2, it is a great challenge to guard against [1–5]. The clinical symptoms of COVID-19 disease include fever, cough, fatigue, shortness of breath, loss of smell and gastrointestinal symptoms, all these are similar to the common symptoms of influenza [6]. What's more, the asymptomatic patients and the ones during the incubation period are also infectious though they show none of mentioned symptoms, they can transmit the virus to the healthy persons [7]. Currently, the COVID-19 disease has posed great danger to the health of mankind and affected the global production and life order seriously, which is even far more destructive than 2003 SARS-CoV. Therefore, a rapid and effective strategy for diagnose of unprecedented COVID-19 at a large scale is of unparalleled significance [8]. At present, real-time reverse-transcriptase polymerase chain reaction (RT-PCR) is regarded as the gold standard method for the diagnosis of COVID-19 [9]. Nevertheless, due to the expensive instruments, the complicated sample operation steps, the lack of the specialized laboratory and the trained personnel, the practical applications of this method is greatly restricted. In comparison, the coronavirus antigen testing is a promising candidate to achieve the detection for SARS-CoV-2, which can overcome the above problems [10]. The nucleocapsid protein, as one of the major structural proteins encoded by SARS-CoV-2 genome, is abundantly expressed during infection [11,12], and is therefore regarded as a biomarker of SARS-CoV-2 in antigen testing [13]. Hence, a sensitive and selective method is critical for SARS-CoV-2 nucleocapsid protein (CoVNP).

Electrochemiluminescence (ECL), a technology combined chemiluminescence with electrochemistry, is induced via the electrochemical redox reaction of luminophores [14–20]. And ECL is considered to be a promising assay method for determination of CoVNP owing to its advantages of low background signals, high sensitivity, simple equipment and electrochemical controllability [21–24]. This advanced technology has been successfully applied in many researched fields including biomarkers detection [25], bio-imaging [26], point-of-care diagnosis [27], as well as DNA and proteins detection [28,29]. In particular, tris (2, 2'-bipyridine) ruthenium (II) ($\text{Ru}(\text{bpy})_3^{2+}$) and its derivatives have acted as ECL reagents on ECL sensors for long time because of their high ECL efficiency. Furthermore, tri-*n*-propylamine (TPA) is always utilized as the coreactant and reacts with $\text{Ru}(\text{bpy})_3^{2+}$ to promote the ECL efficiency [30,31]. Nevertheless, in the pure $\text{Ru}(\text{bpy})_3^{2+}$ /TPA system, $\text{Ru}(\text{bpy})_3^{2+}$ is difficult to immobilize on the surface of electrode because of its good water solubility, which can not only cause $\text{Ru}(\text{bpy})_3^{2+}$ to spill over and disperse freely in solution-phase, but also the consumption of the expensive Ru source [32]. Besides, to achieve good sensitivity, the high concentration of TPA is needed, which can lead to high background for the ECL system [33]. Taking these into consideration, the $\text{Ru}(\text{bpy})_3^{2+}$ /TPA system is still not stable enough to achieve the excellent ECL performance for the ECL cycle. As a result, it remains urgently needed and extremely challenging to explore useful approach to attain a smooth channel for $\text{Ru}(\text{bpy})_3^{2+}$ and TPA in ECL reaction and further boost the ECL performance.

Recently, researchers have committed their much effort to searching and developing high-performance nanostructures to further enhance the ECL efficiency of $\text{Ru}(\text{bpy})_3^{2+}$ /TPA. Two-dimensional (2D) ultrathin bismuth oxychloride (BiOCl), one kind of ternary compound semiconductor, has attracted particular interest because of its good

biocompatibility, high abundance, pleasing photocatalytic efficiency and unique layered structure [34]. Particularly, BiOCl is made up of interlacing $[\text{Bi}_2\text{O}_2]$ slabs with double $[\text{Cl}_2]$ slabs, showing the strong Bi–O (Cl) covalent bonds and weak Cl–Cl van der Waals force [35,36]. Regrettably, the fast charge recombination rate and weak visible light response limit the application of BiOCl. Heteroatom doping is an effective way to improve the property of BiOCl, among various elements, phosphorus (P) is beneficial to the electron-hole separation, interfacial charge transfer and visible light absorption, resulted by its remarkable electron donating capability, applicable radius and variable valence [37]. However, we also find that the ultrathin P-doped BiOCl (P–BiOCl) has some limitations in ECL application on account of its own poor water dispersion and low conductivity. To address the aforementioned issues, it is imperative to develop a powerful supporting platform to anchor P–BiOCl nanosheets and promote the ECL signal intensity.

MXene, a fast-growing family of 2D transitional metal carbides, nitrides and carbonitrides, has become a research hotspot since first reported by Gogotsi and his co-workers in 2011 [38]. Strikingly, MXene not only possesses well-defined layered architectures, muscular mechanical rigidity, superior stability, the active metal centers, but also high surface area. Owing to the outstanding physicochemical characteristics, MXene has exhibited satisfactory performance in various researched fields over the past decade, including supercapacitors [39, 40], catalysis [41], ion batteries [42–44], solar cells [45], water purification [46], electromagnetic interference shielding [47], sensors [48, 49] and so on. The most remarkable thing is that, research evidences show that the MXene based interfacial heterostructure materials are ideal candidates to fabricate effective ECL biosensors in recent years. For example, Yuan's group reports Ru-complex-grafted MXene nanosheets as an ECL indicator to fabricate ECL sensing platform for the tumor biomarker Mucin 1 (MUC1) [50]. Besides, Yang et al. prepare electroactive and catalytic 2D/2D $\text{Ti}_3\text{C}_2\text{T}_x/\text{TiO}_2$ hybrids to accelerate the electro-oxidation of TPA and $\text{Ir}(\text{ppy})_2(\text{acac})$, the developed immunosensor shows high ECL efficiency in the determination of neuron-specific enolase (NSE) [51]. Inspired by the above innovations, we speculate that MXene is a good scaffold for P–BiOCl, and the formation of rich terminating surface groups (i.e., =O, –OH, and –F) on MXene after exfoliation can help the P–BiOCl easily attach on MXene [40,52,53].

Within this context, we design a 2D/2D MXene/P–BiOCl/ $\text{Ru}(\text{bpy})_3^{2+}$ heterojunction composite to construct a ECL biosensor platform for CoVNP. As displayed in Scheme 1, the synthesis and delamination of $\text{Ti}_3\text{C}_2\text{T}_x$ MXene is realized by in situ HF-generation and sonication exfoliation, then P–BiOCl and $\text{Ru}(\text{bpy})_3^{2+}$ are anchored on MXene through solvothermal method and electrostatic interaction successively. Remarkably, MXene/P–BiOCl/ $\text{Ru}(\text{bpy})_3^{2+}$ showcases intrinsic high electrochemical conductivity, hydrophilicity, good biocompatible, enriched terminating surface groups and high electrochemical active surface. In this protocol, the as-prepared MXene/P–BiOCl/ $\text{Ru}(\text{bpy})_3^{2+}$ hybrids are modified on the electrode to immobilize Anti-2019-nCoV-N McAb (Ab) and CoVNP. The ECL efficiency has been greatly promoted with MXene/P–BiOCl/ $\text{Ru}(\text{bpy})_3^{2+}$ /GCE in the presence of TPA as the coreactant for ECL “signal on”. Concretely, the generation of the stronger ECL signal intensity is because MXene/P–BiOCl/ $\text{Ru}(\text{bpy})_3^{2+}$ can electrocatalyze the oxidation of TPA and greatly promoted the produce of intermediate TPA^* , which also demonstrates that MXene/P–BiOCl/ $\text{Ru}(\text{bpy})_3^{2+}$ is an efficient signal amplifier and coreaction accelerator. Ultimately, the target CoVNP specifically binds to the MXene/P–BiOCl/ $\text{Ru}(\text{bpy})_3^{2+}$ heterojunction composite, realizing the ECL intensity decrease of MXene/P–BiOCl/ $\text{Ru}(\text{bpy})_3^{2+}$ -TPA system for ECL “signal off”. As expected, the developed ECL biosensor for CoVNP recognition

possesses highly sensitive and selective ECL performance. Moreover, this sensor showcases excellent practical applicability in human serum. Notably, the combination of 2D MXene architectures and 2D semiconductor materials will guide for the design of high performance ECL biosensors, and it is valuable for the diagnosis and treatment of various diseases.

2. Experimental section

2.1. Preparation of $Ti_3C_2T_x$ MXene

Firstly, the multilayered $Ti_3C_2T_x$ ($m-Ti_3C_2T_x$) MXene is prepared via the selective etching of Al element from the raw material Ti_3AlC_2 with in situ HF-generation. Specifically, 1.6 g of LiF is mixed with 20 mL of HCl (9 M) uniformly with constant stirring. Next, 1 g of Ti_3AlC_2 is added to the above etching solution and the reaction proceeds at 40 °C for 24 h. The obtained product is centrifuged and washed several times with deionized water till the supernatant pH > 6. Then, the prepared $m-Ti_3C_2T_x$ MXene is dispersed in deionized water by ultrasonic treatment for 1 h under argon protection to avoid the oxidation of MXene. Finally, the single-layered $Ti_3C_2T_x$ ($s-Ti_3C_2T_x$) MXene is collected by centrifugation.

2.2. Preparation of MXene/P-BiOCl/Ru(bpy) $_3^{2+}$

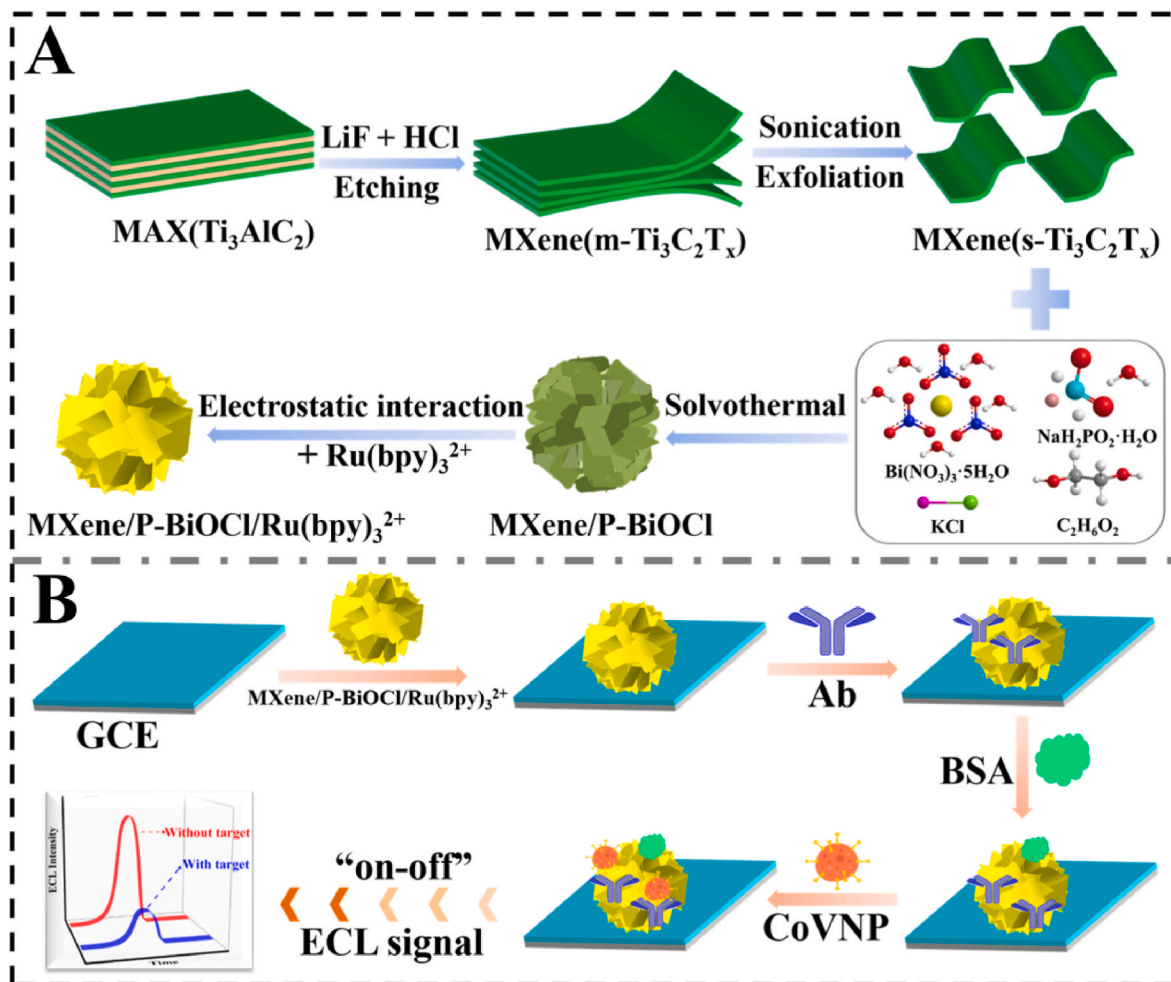
The preparation of the 2D/2D MXene/P-BiOCl is performed via a solvothermal process according to a reported work with minor

modifications [37]. Firstly, 5 mmol of $Bi(NO_3)_3 \cdot 5H_2O$ is dissolved in 40 mL of ethylene glycol ($C_2H_6O_2$) with magnetically stirring to obtain transparent solution. Secondly, 5 mmol of KCl and 0.5 mmol of $NaH_2PO_2 \cdot H_2O$ are dispersed in a beaker containing 10 mL of deionized water. Subsequently, the latter solution is added dropwise into the former one and kept continuous stirring for 1 h. Next, 1 mL of 5 mg/mL $s-Ti_3C_2T_x$ MXene dispersion is introduced into the above sufficiently mixed solution under stirring and kept for another 2 h. Then, transferring the resultant suspension into the 80 mL Teflon-lined autoclave and maintained at 180 °C for 24 h. After the solvothermal reaction, the resulting samples are centrifuged and washed several times with deionized water, ethanol and then dried at 60 °C. The product is named as MXene/P-BiOCl.

For comparison, P-BiOCl is prepared without introduction of $s-Ti_3C_2T_x$ MXene dispersion. For the synthesis of MXene/P-BiOCl/Ru(bpy) $_3^{2+}$, 5 mM of Ru(bpy) $_3^{2+}$ is dispersed with MXene/P-BiOCl in deionized water with magnetically stirring for 12 h, MXene/P-BiOCl/Ru(bpy) $_3^{2+}$ is self-assembled via the electrostatic interaction. The obtained MXene/P-BiOCl/Ru(bpy) $_3^{2+}$ is dried at 60 °C for the later experiment. Besides, P-BiOCl/Ru(bpy) $_3^{2+}$ and MXene/Ru(bpy) $_3^{2+}$ are prepared with the same method.

2.3. Fabrication of ECL biosensor

Before use, the glassy carbon electrode (GCE, 3 mm in diameter) is polished with 1.0 μm and 0.2~0.5 μm Al_2O_3 powder, and is cleaned with deionized water and ethanol under sonication. 5 mg of MXene/



Scheme 1. Schematic illustration of (A) preparation of MXene/P-BiOCl/Ru(bpy) $_3^{2+}$. (B) assembly procedure of a "signal on-off" ECL biosensor for CoVNP.

P-BiOCl/Ru(bpy)₃²⁺ is dissolved into 40 μL of ethanol and 10 μL of Nafion 117 (1%) to prepare the ink. Subsequently, the GCE is modified with 5 μL of MXene/P-BiOCl/Ru(bpy)₃²⁺ ink. Then, 5 μL of 20 μg/mL Anti-2019-nCoV-N McAb (Ab) is covalently immobilized on the surface of the electrode via Bi-O bond of MXene/P-BiOCl/Ru(bpy)₃²⁺ [36] to form Ab/MXene/P-BiOCl/Ru(bpy)₃²⁺ and is fostered at 37 °C for 60 min. To block the nonspecific site, 5 μL 1% the bovine serum albumin (BSA) is further coated on the electrode at 37 °C overnight for guaranteeing the specific interaction of Ab toward CoVNP. Finally, 5 μL of distinct concentrations of the target CoVNP is introduced and incubated at 37 °C for 60 min. What's noteworthy is that, every step is followed by phosphate buffer solution (PBS) washing to remove excess impurities. The as-prepared ECL biosensor MXene/P-BiOCl/Ru(bpy)₃²⁺/GCE is stored at 4 °C in a refrigerator for further use.

2.4. Electrochemistry and ECL measurements

Cyclic voltammetry (CV) and electrochemical impedance spectroscopy (EIS) measurements are tested in 5.0 mM [Fe(CN)₆]³⁻/[Fe(CN)₆]⁴⁻ with 0.1 M KCl. ECL experiments are performed in 0.1 M PBS (pH = 7.4) containing 0.1 M KCl and 5 mg/mL of TPA, with the potential range is from 0.2 to 1.25 V, the scanning rate is 100 mV/s and the photomultiplier tube (PMT) at 800 V. In all experiments, the modified GCE, saturated Ag/AgCl electrode (sat. KCl) and platinum wire electrode are acted as working electrode, reference electrode and counter electrode, respectively.

3. Results and discussion

3.1. Characterization of MXene/P-BiOCl/Ru(bpy)₃²⁺

The phase structure and morphology of the MXene/P-BiOCl/Ru(bpy)₃²⁺ heterojunctions are first confirmed. The X-ray diffraction (XRD) patterns of Ti₃AlC₂, MXene, P-BiOCl, MXene/P-BiOCl and MXene/P-BiOCl/Ru(bpy)₃²⁺ are displayed in Fig. 1A, all these substances have good crystallinity. The diffraction peaks of Ti₃AlC₂ can match with (PDF card 52-0875), and those of Ti₃C₂T_x MXene after etching and exfoliation are in correspondence with the reported work [50]. The peaks of P-BiOCl shift slightly compared with those of BiOCl (PDF card 06-0249), resulted by the doping of P heteroatoms. Besides, it can be

seen that the characteristic diffraction peaks are found in MXene/P-BiOCl and MXene/P-BiOCl/Ru(bpy)₃²⁺. The morphologies of the prepared nanomaterials are characterized by scanning electron microscopy (SEM). As exhibited in Fig. S1A, Ti₃AlC₂ presents a tightly stacked morphology. Figs. S1B and S1C and Fig. 1B show that MXene after etching and exfoliation has larger interlayer spacing compared with Ti₃AlC₂. In Fig. S2, by shining a laser beam, a clear Tyndall Effect is observed in the s-Ti₃C₂T_x MXene dispersion, in stark contrast to the deionized water, demonstrating the existence of a colloidal suspension. The SEM images of P-BiOCl indicate that it is a 2D sheet-like nanostructure with the stacked distribution, as depicted in Figs. S1D and S1E. Furthermore, when P-BiOCl nanosheets grow on the surface of MXene through solvothermal method, the self-assembled 2D/2D MXene/P-BiOCl heterojunction can be obtained (Fig. 1C, D, E). In addition, Fig. 1F confirms that Ru(bpy)₃²⁺ has also anchored on the MXene/P-BiOCl by the electrostatic interaction.

To further investigate the microstructures of the composites, transmission electron microscope (TEM) and high-resolution TEM (HRTEM) are performed. The TEM image shown in Fig. 2A verifies that the heterojunctions are formed by layered MXene, 2D sheet-like P-BiOCl and Ru(bpy)₃²⁺ components. As illustrated in Fig. 2B, the highly resolved lattice spacing of 0.344, 0.230, 0.173 and 0.163 nm are observed in the HRTEM image, agreement with the (101) plane of BiOCl, (104), (108) and (109) planes of Ti₃C₂T_x MXene, and 0.357 nm is the (112) plane of Ru from Ru(bpy)₃²⁺ [54]. In Fig. 2C, Energy dispersive spectrometer (EDS) elemental mapping images including Bi, Ru, Ti, O, C, N, Cl, F and P elements, which are homogeneously distributed on the surface of the MXene/P-BiOCl/Ru(bpy)₃²⁺. Above characterizations reveal that MXene/P-BiOCl/Ru(bpy)₃²⁺ heterojunctions have been successfully prepared.

The surface elemental composition and chemical states of as-synthesized MXene/P-BiOCl/Ru(bpy)₃²⁺ are evaluated by X-ray photoelectron spectroscopy (XPS). Fig. 3A displays the XPS survey spectrum of MXene/P-BiOCl/Ru(bpy)₃²⁺. Bi 4f XPS spectrum is presented in Fig. 3B, the peaks at 163.9 and 158.6 eV are attributed to Bi 4f_{5/2} and Bi 4f_{7/2}, respectively. As shown in Fig. 3C, the peaks appearing at 284.5 and 280.8 eV refer to the binding energies of Ru 3d_{3/2} and Ru 3d_{5/2}, respectively. Fig. 3D exhibits the Ti 2p spectrum for MXene/P-BiOCl/Ru(bpy)₃²⁺, two peaks at 466.7 and 464.0 eV are corresponding to the lattice Ti-O binding in TiO₂. The peaks located at 465.4 and 459.1 eV

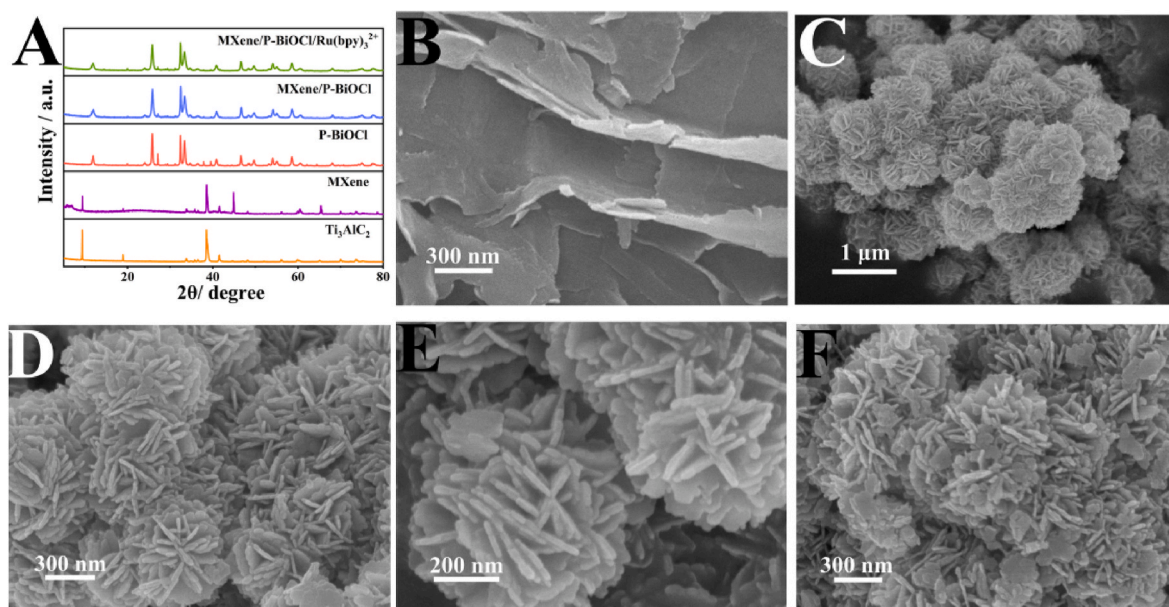


Fig. 1. (A) XRD patterns of Ti₃AlC₂, MXene, P-BiOCl, MXene/P-BiOCl and MXene/P-BiOCl/Ru(bpy)₃²⁺. High SEM magnification images of MXene (B). Low (C) and high (D), (E) magnification SEM images of MXene/P-BiOCl. SEM images of MXene/P-BiOCl/Ru(bpy)₃²⁺ (F).

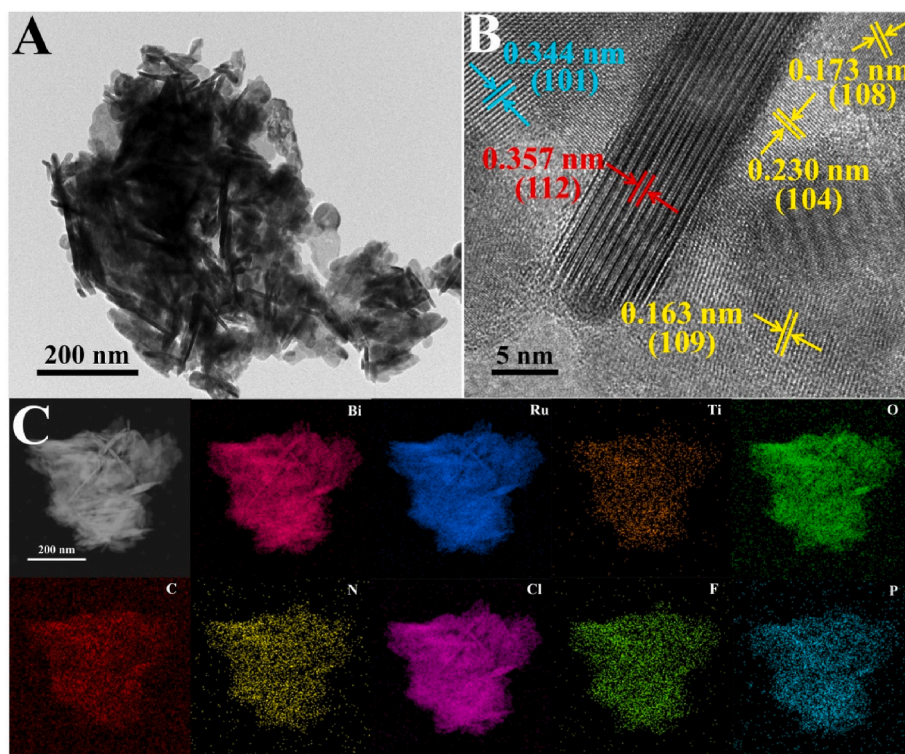


Fig. 2. (A) TEM and (B) HRTEM images of MXene/P-BiOCl/Ru(bpy)₃²⁺. (C) EDS element mapping images of MXene/P-BiOCl/Ru(bpy)₃²⁺.

are attributed to Ti-X, the characteristic peak of Ti_xO_y is at 462.0 eV, and the peak at 448.2 eV is ascribed to the Ti-C. The C 1s peaks in Fig. S3E at 288.4, 284.6 and 280.9 eV are assignable to O=C-O, C=C and C-Ti, respectively. There are two peaks at 199.0 eV to Cl 2p_{1/2} and 197.4 eV to Cl 2p_{3/2} for Cl⁻ (Fig. 3F). And P-O bond at 132.6 eV is found in P 2p (Fig. 3G). The O 1s XPS spectra of MXene/P-BiOCl/Ru(bpy)₃²⁺ show three typical peaks, specifically, 532.5 eV to O=C, 530.7 eV to Ti-O, and 529.4 eV O-Bi (Fig. 3H). As depicted in Fig. 3I, the peak at 399.5 eV is identified as C-N bond. These characterizations verify the successful incorporation of P-BiOCl and Ru(bpy)₃²⁺ into the synthesized MXene.

Fig. S3A compares the UV-visible diffuse reflectance spectra (UV-vis DRS) of P-BiOCl, MXene, MXene/P-BiOCl and MXene/P-BiOCl/Ru(bpy)₃²⁺. Three peaks at 450 nm, 290 nm and 230 nm are ascribed to MXene/P-BiOCl/Ru(bpy)₃²⁺, corresponding to the characteristic absorption peaks of Ru(bpy)₃²⁺, MXene and P-BiOCl, confirming the successful preparation of heterojunctions. Fourier transform infrared (FT-IR) spectroscopy is adopted to further verify the formation of MXene/P-BiOCl/Ru(bpy)₃²⁺. As displayed in Fig. S3B, MXene/P-BiOCl/Ru(bpy)₃²⁺ presents a large broad peak at 3280-3660 cm⁻¹ in the FT-IR spectrum, assigned to the O-H groups stretching vibration. With the introduction of MXene and Ru(bpy)₃²⁺, the peaks at 1620 cm⁻¹ and 1452 cm⁻¹ blue shift, caused by the interaction of three components. Besides, the fluorescence (FL) excitation and emission spectra of MXene/P-BiOCl/Ru(bpy)₃²⁺ present peaks at 449 nm and 653 nm, respectively (Fig. S3C).

3.2. Conductivity-enhanced ECL investigation of MXene/P-BiOCl/Ru(bpy)₃²⁺

CV and the Nyquist plots recorded by EIS is adopted to validate the interfacial natures and conductivities of various materials in 5.0 mM [Fe(CN)₆]³⁻/[Fe(CN)₆]⁴⁻ with 0.1 M KCl. As depicted in Fig. S4A, when different materials modifying on the GCE, there is the strongest current on MXene/P-BiOCl/Ru(bpy)₃²⁺/GCE except the bare GCE, resulted by the superior electrical conductivity of MXene/P-BiOCl/Ru(bpy)₃²⁺. From Fig. S4B, we find that MXene/P-BiOCl/Ru(bpy)₃²⁺/GCE presents

the smallest electron transfer resistance (*R*_{et}) value, indicating the outstanding ability of promoting the electron transfer. As can be seen from Figs. S4C and S4D, in the ECL measurements of different materials, MXene/P-BiOCl/Ru(bpy)₃²⁺ (curve f) shows the best ECL signal intensity compared with the bare GCE (curve a), P-BiOCl/GCE (curve b) and MXene/P-BiOCl/GCE (curve c), P-BiOCl/Ru(bpy)₃²⁺/GCE (curve d) and MXene/Ru(bpy)₃²⁺/GCE (curve e), because of the competent ECL property of MXene/P-BiOCl/Ru(bpy)₃²⁺. We also compare the property of the GCE and Au electrode, the corresponding ECL intensity-potential curves in Fig. S5 reveal that the GCE is superior to the Au electrode.

3.3. Electrochemical and ECL performance of the sensing platform

To characterize the fabrication procedure of the biosensor step by step, techniques including CV, EIS and ECL are conducted. As described in Fig. 4A, the largest redox peak presents on the bare GCE (curve a), whereas the redox peak current decreases dramatically when the GCE is modified by the binder Nafion (curve b), which can contribute to the poor conductivity of the binder. After the nanocomposites MXene/P-BiOCl/Ru(bpy)₃²⁺ decorating on the electrode (curve c), the current obviously increases due to its brilliant conductivity. Subsequently, it is readily see that the electrochemical signals continuously reduce with Ab (curve d), BSA (curve e) and CoVNP (curve f) stepwise incubating on MXene/P-BiOCl/Ru(bpy)₃²⁺/GCE, because of the non-conductivities of biomacromolecules [17].

Additionally, the corresponding EIS characterizations of the assembled biosensors are exhibited in Fig. 4B. The *R*_{et} value of MXene/P-BiOCl/Ru(bpy)₃²⁺/GCE (curve b) is much smaller than that of the bare GCE (curve a), forcefully demonstrating MXene/P-BiOCl/Ru(bpy)₃²⁺ can improve the electron transfer. Then, along with the successive incubation of Ab (curve c), BSA (curve d) and CoVNP (curve e), the semicircle diameter increases gradually, because the electronically inert feature of biomacromolecules can block the electron transfer.

The ECL responses of the biosensor construction process are also recorded. As can be seen from Fig. 4C, both of the bare GCE (curve a) and the Nafion/GCE (curve b) show extremely weak ECL signals. As

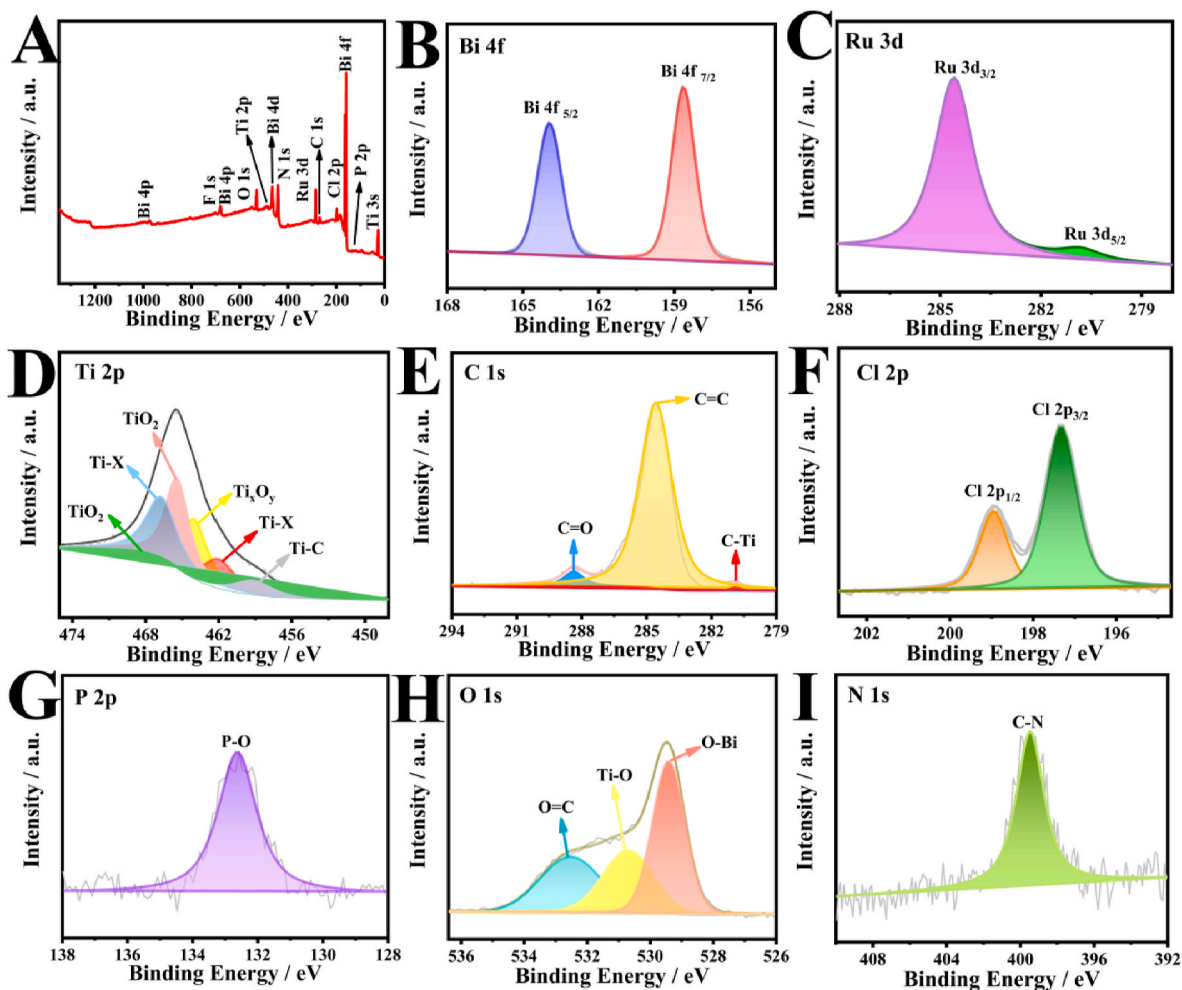


Fig. 3. (A) XPS survey spectrum of MXene/P-BiOCl/Ru(bpy)₃²⁺ heterojunction and core-level spectra of Bi 4f (B), Ru 3d (C), Ti 2p (D), C 1s (E), Cl 2p (F), P 2p (G), O 1s (H), and N1s (I).

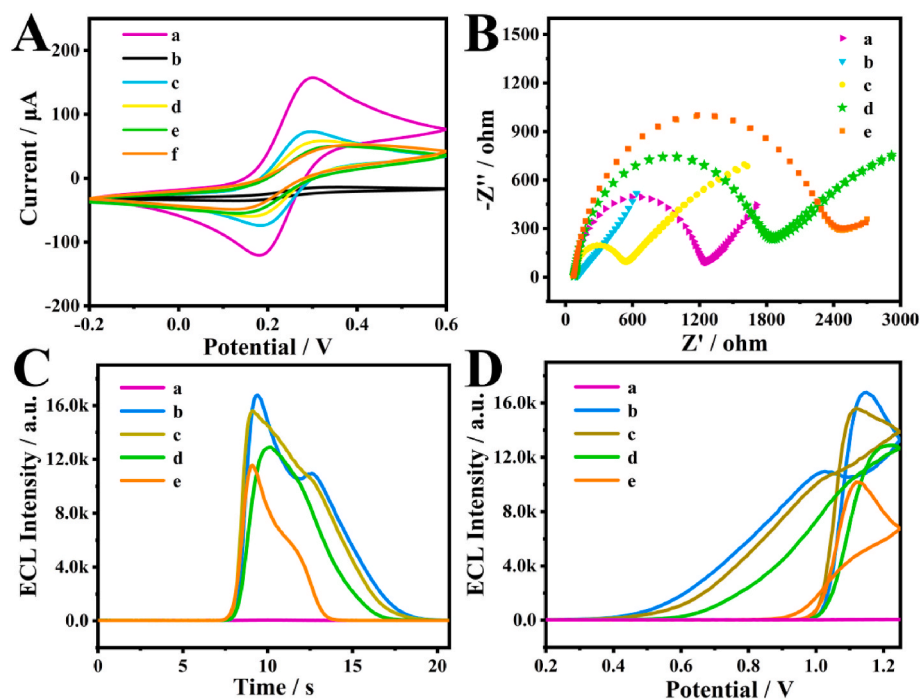
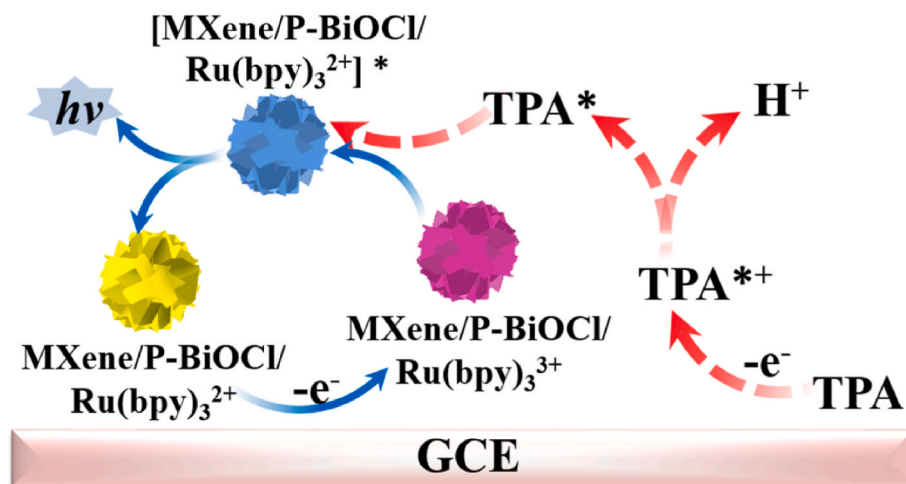
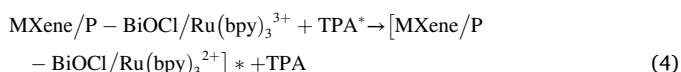
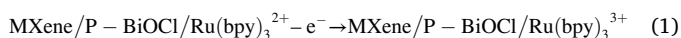


Fig. 4. Characterizations of stepwise fabrication of the biosensor (A) CV curves of (a) bare GCE, (b) Nafion/GCE, (c) MXene/P-BiOCl/Ru(bpy)₃²⁺/GCE, (d) Ab/MXene/P-BiOCl/Ru(bpy)₃²⁺/GCE, (e) BSA/Ab/MXene/P-BiOCl/Ru(bpy)₃²⁺/GCE, (f) 1 fg/mL CoVNP/BSA/Ab/MXene/P-BiOCl/Ru(bpy)₃²⁺/GCE, at scan rate of 50 mV/s (B) EIS characterizations, (C) ECL intensity responses and (D) ECL intensity-potential curves of (a) bare GCE, (b) MXene/P-BiOCl/Ru(bpy)₃²⁺/GCE, (c) Ab/MXene/P-BiOCl/Ru(bpy)₃²⁺/GCE, (d) BSA/Ab/MXene/P-BiOCl/Ru(bpy)₃²⁺/GCE, (e) 1 fg/mL CoVNP/BSA/Ab/MXene/P-BiOCl/Ru(bpy)₃²⁺/GCE.

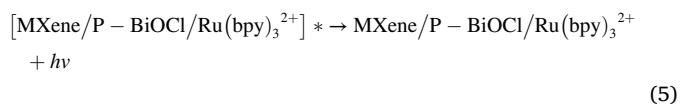
expected, the strongest ECL intensity presents on MXene/P-BiOCl/Ru(bpy)₃²⁺/GCE (curve c) on account of the excellent ECL performance of MXene/P-BiOCl/Ru(bpy)₃²⁺. However, when the MXene/P-BiOCl/Ru(bpy)₃²⁺/GCE is sequentially anchored with Ab (curve d), BSA (curve e) and CoVNP (curve f), the ECL signal gradually decreases. ECL intensity-potential curves in Fig. 4D show the same trend with Fig. 4C. All the experimental results of CV, EIS and ECL indicate that the proposed ECL biosensor has been successfully developed.

3.4. ECL mechanism exploration

The constructed ECL biosensor based on MXene/P-BiOCl/Ru(bpy)₃²⁺ is employed as the specific recognition platform throughout the whole experiment, and the coreactant TPA is introduced to enhance the ECL intensity. Initially, when the prepared MXene/P-BiOCl/Ru(bpy)₃²⁺ ink is decorated onto the surface of GCE, in turn, a strong initial ECL signal intensity is generated in the presence of TPA as the coreactant for ECL “signal on”. Hereafter, CoVNP binds to the specific site of Ab, ultimately, when achieving the attachment of the plentiful target CoVNP on the electrode, electron transfer is blocked with remarkable ECL quenching for “signal off”. The working mechanism of “signal on-off” is explicated through the electron transfer procedure as displayed in Scheme 2. Referring to the reported works [30], the possible ECL mechanism of MXene/P-BiOCl/Ru(bpy)₃²⁺ is proposed as eqs (1)–(5). First of all, MXene/P-BiOCl/Ru(bpy)₃²⁺ and TPA lose electrons and are oxidized to MXene/P-BiOCl/Ru(bpy)₃³⁺ and TPA^{•+} in electrochemical reaction (eqs (1) and (2)). In addition, as MXene/P-BiOCl/Ru(bpy)₃³⁺ has greatly promoted the produce of TPA^{•+}, the ECL intensity is obviously enhanced. Then, TPA^{•+} deprotonates and becomes the intermediate TPA* (eq (3)). Further, the ECL signal is obtained through the generation of the excited state [MXene/P-BiOCl/Ru(bpy)₃²⁺]* and TPA, realized by the electron transfer between [MXene/P-BiOCl/Ru(bpy)₃³⁺] and TPA* (eq (4)). Subsequently, the excited state [MXene/P-BiOCl/Ru(bpy)₃²⁺]* returns to the ground state MXene/P-BiOCl/Ru(bpy)₃²⁺ and releases photons (eq (5)).



Scheme 2. Schematic of ECL mechanism of MXene/P-BiOCl/Ru(bpy)₃²⁺-TPA system.



Moreover, CV technique is carried out to study the electrochemical process of MXene/P-BiOCl/Ru(bpy)₃²⁺ in 0.1 M PBS (pH 7.4) at various scan rates (from 25 to 200 mV/s). As presented in Fig. S6, both anodic and cathodic peak currents show a great linear relationship to the square root of scan rates, the linear equations are $I_{pa} = 1.232 + 0.3432 v^{1/2}$ ($R^2 = 0.997$), $I_{pc} = 0.7532 - 0.2249 v^{1/2}$ ($R^2 = 0.999$), respectively, which proves that MXene/P-BiOCl/Ru(bpy)₃²⁺ undergo a diffusion-controlled process.

3.5. Optimization of experimental conditions

In order to obtain the satisfactory detection results, some main parameters that play vital roles for the detection efficiency are optimized, including pH value of PBS, incubation temperature, incubation time and concentration of Ab. As protein is highly sensitive to the pH of its surrounding environment, we investigate the compatibility of the biosensor to various pH conditions (ranging from 6.0 to 8.0). In Fig. S7A, the ECL intensity shows the best result as pH is 7.4, so the subsequent experiments are carried out at pH 7.4. As displayed in Fig. S7B, when the incubation temperature changes from 18 °C to 45 °C, the ECL signal gradually attenuates and tends to be stable until 37 °C. In view of 37 °C is close to the normal body temperature, so we do not select too high temperature as the optimal incubation temperature for the subsequent experiments. Therefore, 37 °C is considered to be as the best incubation temperature. Meanwhile, the effect of the incubation time for CoVNP should not be overlooked. Fig. S7C shows the ECL intensity decreases with the increasing of incubation time and reaches a plateau at 60 min, implying 60 min is the perfect time in our ECL strategy. Furthermore, the ECL intensity of the biosensor with the concentration of COVID-19 Ab is also explored, Fig. S7D shows that 20 µg/mL of Ab is optimal for the ECL performance of the developed biosensor.

3.6. ECL response of the biosensor towards CoVNP

To assess the analytical performance of the prepared ECL biosensor, different concentrations of CoVNP are determined under the optimal experimental condition. As displayed in Fig. 5A, the ECL response decreases gradually with the increment of the concentration of CoVNP enhancing from 1 fg/mL to 10 ng/mL. To our satisfaction, the ECL signal intensity presents a perfect linear relationship with the logarithm of the

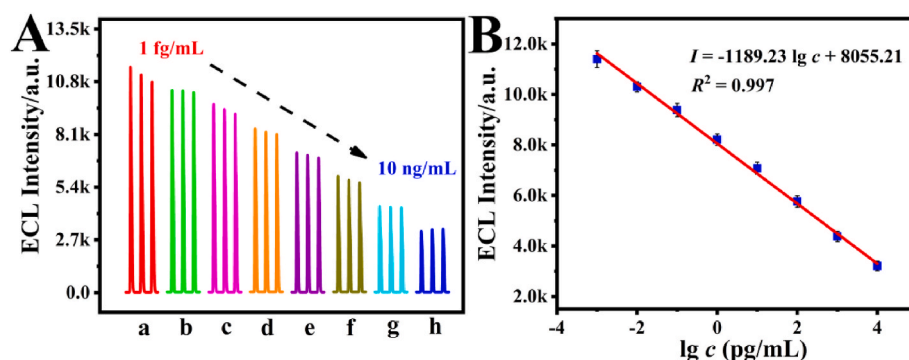


Fig. 5. (A) ECL intensities of the constructed ECL biosensor with different concentrations of CoVNP (a) to (h): 1.0, 10, 100 fg/mL; 1.0, 10, 100 pg/mL; 1.0 and 10 ng/mL. (B) Linear relationship between ECL response and logarithm of the concentration CoVNP.

concentration of CoVNP shown in Fig. 5B, the corresponding linear regression equation is described as $I = -1189.23 \lg c + 8055.21$ ($R^2 = 0.997$), the obtained limit of detection (LOD) is calculated to be 0.49 fg/mL ($S/N = 3$). Besides, we also compare the ECL performance of Ru(bpy) $_3^{2+}$ /TPA with MXene/P-BiOCl/Ru(bpy) $_3^{2+}$ /TPA. As presented in Fig. S8, the results show MXene/P-BiOCl/Ru(bpy) $_3^{2+}$ has strong and steady signal output both for the detection of 0 pg/mL and 10 pg/mL CoVNP in 0.1 M PBS (pH 7.4) containing 0.1 M KCl and 5 mg/mL of TPA, which verify the superiority of our constructed ECL immunosensor than the mentioned Ru(bpy) $_3^{2+}$ /TPA.

In addition, as listed in Table S1, as-constructed biosensor exhibits comparable or superior performance in determination for COVID-19 disease compared with other recently reported bioassay method. The excellent performance of the proposed detection method can be ascribed to that the heterojunctions MXene/P-BiOCl/Ru(bpy) $_3^{2+}$ can not only act as excellent accelerators of TPA, but also synergistically quench the ECL intensity.

3.7. Specificity, reproducibility and stability of the ECL biosensor

Specificity, reproducibility and stability are critical indicators for evaluating the properties of the established ECL biosensor. The specificity test is studied via employing different interferences including carcino-embryonic antigen (CEA), beta-human chorionic gonadotropin (HCG), neuron specific enolase (NSE) as well as prostate specific antigen (PSA) at the concentration of 10 ng/mL. As depicted in Fig. 6A, the ECL intensities of the mentioned interferences exhibit no significant differences to the blank sample. Besides, negligible differences of ECL responses are presented when detecting the mixture solution (10 ng/mL CEA, 10 ng/mL HCG, 10 ng/mL NSE, 10 ng/mL PSA and 1 ng/mL CoVNP) and the target 1 ng/mL CoVNP alone. To investigate the reproducibility of the sensor, the fabricated electrode is adopted to detect five parallel samples incubated with 10 fg/mL CoVNP. As shown in Fig. 6B, the ECL intensities display little variation with the relative

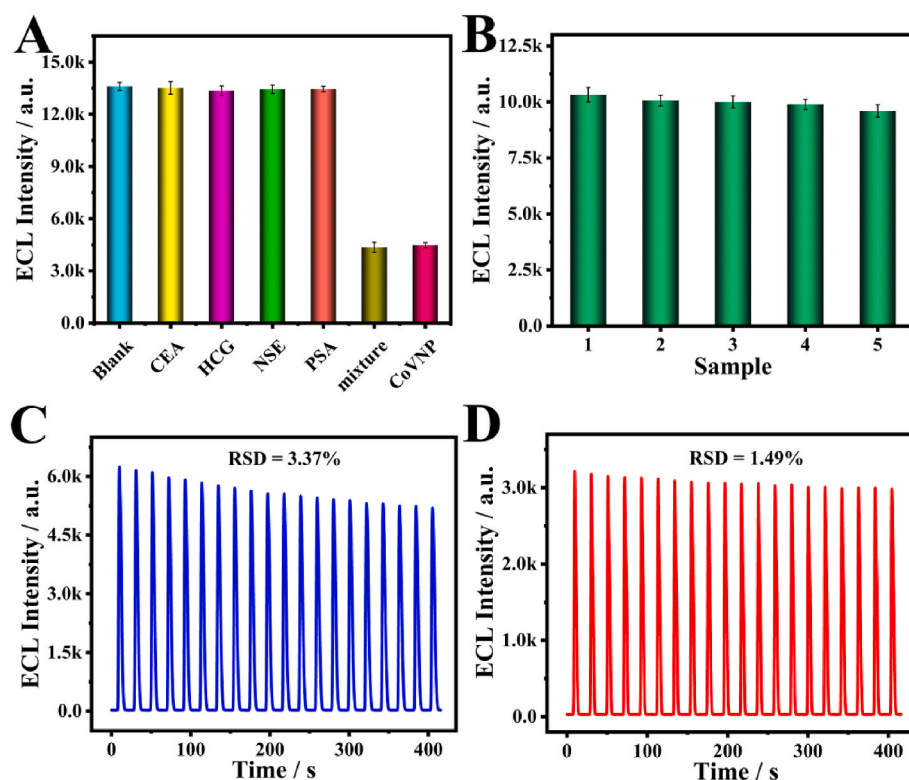


Fig. 6. (A) Specificity of the ECL biosensor against different substances: blank solution, 10 ng/mL CEA, 10 ng/mL HCG, 10 ng/mL NSE, 10 ng/mL PSA, mixture substances containing 1 ng/mL CoVNP and 1 ng/mL CoVNP alone. (B) Reproducibility of the fabricated biosensor toward five parallel samples incubated with 10 fg/mL COVID-19 At. (C) Stability of the ECL biosensor with 100 pg/mL, (D) 10 ng/mL COVID-19 At under 20 consecutive cycles scans.

standard deviation (RSD) of 2.64%, revealing excellent reproducibility of the fabricated sensor. Moreover, the operational stability tests are implemented by recording the ECL signals of different concentrations of CoVNP under 20 cycles consecutive scanning. And the results are presented in Fig. 6C and D, the ECL intensities show no significant change, the RSD are 3.37% for 100 pg/mL CoVNP and 1.49% for 10 ng/mL CoVNP respectively, which confirms that the ECL biosensor is endowed with superior stability.

3.8. Application in serum sample analysis

With the purpose of further validating the feasibility of the developed ECL biosensor in clinical application, the recovery studies are performed in human serum for CoVNP detection with the standard addition method. As displayed in Table S2, the recoveries of the ECL sensor are in the range of 93.0%–99.5%, and the RSD is within 5%. It means that our proposed MXene/P–BiOCl/Ru(bpy)₃²⁺/GCE ECL biosensor platform has satisfactory reliability and practical applicability.

4. Conclusions

In conclusion, the 2D/2D MXene/P–BiOCl nanocomposite is a desired candidate to provide a smooth channel for Ru(bpy)₃²⁺ and TPA in ECL reaction and promote the ECL performance for the ECL cycle. Besides, MXene/P–BiOCl/Ru(bpy)₃²⁺ can electrocatalyze the oxidation of TPA and greatly promoted the produce of intermediate TPA*, highlighting that MXene/P–BiOCl/Ru(bpy)₃²⁺ is an efficient signal amplifier and co-reaction accelerator. Based on the MXene/P–BiOCl/Ru(bpy)₃²⁺-TPA system, the developed “signal on-off” ECL biosensor performs the reliable recognition for CoVNP, obtaining a wide linear range from 1 fg/mL to 10 ng/mL and a low LOD of 0.49 fg/mL (S/N = 3). In addition, the combination of 2D MXene architectures with 2D semiconductor materials has potential to construct high-performance ECL sensing platforms. This work presents a new perspective for the applications of ECL in the nanomedicine field and clinical practice, preventing various diseases and guarding the health of mankind.

CRediT authorship contribution statement

Xuebo Liu: Conceptualization, Data curation, Writing – original draft. **Liwei Bai:** Validation, Formal analysis. **Xiaowei Cao:** Formal analysis, Methodology. **Feng Wu:** Formal analysis, Review & editing. **Tao Yin:** Validation. **Wenbo Lu:** Methodology, Project administration, Review & editing, Funding acquisition, Supervision.

Declaration of competing interest

The authors declare that they have no known competing financial interests or personal relationships that could have appeared to influence the work reported in this paper.

Data availability

The data that has been used is confidential.

Acknowledgments

This work was supported by the National Natural Science Foundation of China (No. 21705103), the Applied Basic Research Project of Shanxi Province (No. 202103021224251), Scientific and Technological Innovation Projects in Shanxi Universities (No.2019L0460), the Graduate Education Innovation Project of Shanxi Province (2021Y485), and the 1331 Engineering of Shanxi Province.

Appendix B. Supplementary data

Supplementary data to this article can be found online at <https://doi.org/10.1016/j.aca.2022.340522>.

References

- [1] F. Wu, S. Zhao, B. Yu, Y. Chen, W. Wang, Z. Song, Y. Hu, Z. Tao, J. Tian, Y. Pei, M. Yuan, Y. Zhang, F. Dai, Y. Liu, Q. Wang, J. Zheng, L. Xu, E. Holmes, Y. Zhang, A new coronavirus associated with human respiratory disease in China, *Nature* 579 (2020) 265–269.
- [2] P. Zhou, X. Yang, X. Wang, B. Hu, L. Zhang, W. Zhang, H. Si, Y. Zhu, B. Li, C. Huang, H. Chen, J. Chen, Y. Luo, H. Guo, R. Jiang, M. Liu, Y. Chen, X. Shen, X. Wang, X. Zheng, K. Zhao, Q. Chen, F. Deng, L. Liu, B. Yan, F. Zhan, Y. Wang, G. Xiao, Z. Shi, A pneumonia outbreak associated with a new coronavirus of probable bat origin, *Nature* 579 (2020) 270–273.
- [3] Q. Li, X. Guan, P. Wu, X. Wang, L. Zhou, Y. Tong, R. Ren, K. Leung, E. Lau, J. Wong, X. Xing, N. Xiang, Y. Wu, C. Li, Q. Chen, D. Li, T. Liu, J. Zhao, M. Liu, W. Tu, C. Chen, L. Jin, R. Yang, Q. Wang, S. Zhou, R. Wang, H. Liu, Y. Luo, Y. Liu, G. Shao, H. Li, Z. Tao, Y. Yang, Z. Deng, B. Liu, Z. Ma, Y. Zhang, G. Shi, T. Lam, J. Wu, G. Gao, B. Cowling, B. Yang, G. Leung, Z. Feng, Early transmission dynamics in Wuhan, China, of novel coronavirus-infected pneumonia, *N. Engl. J. Med.* 382 (2020) 1199–1207.
- [4] L. Wu, X. Wang, C. Wu, X. Cao, T. Tang, H. Huang, X. Huang, Ultrasensitive SARS-CoV-2 diagnosis by CRISPR-based screen-printed carbon electrode, *Anal. Chim. Acta* 1221 (2022) 340120–340128.
- [5] M. Choi, J. Lee, Y. Seo, Combined recombinase polymerase amplification/rkDNA-graphene oxide probing system for detection of SARS-CoV-2, *Anal. Chim. Acta* 1158 (2021) 338390–338396.
- [6] R. Nouri, Z. Tang, M. Dong, T. Liu, A. Kshirsagar, W. Guan, CRISPR-based detection of SARS-CoV-2: a review from sample to result, *Biosens. Bioelectron.* 178 (2021) 113012–113020.
- [7] Y. Tang, J. Schmitz, D. Persing, C. Stratton, Laboratory diagnosis of COVID-19: current issues and challenges, *J. Clin. Microbiol.* 58 (2020), 00512-00520.
- [8] W. Feng, A. Newbigging, C. Le, B. Pang, H. Peng, Y. Cao, J. Wu, G. Abbas, J. Song, D. Wang, M. Cui, J. Tao, D. Tyrrell, X. Zhang, H. Zhang, X. Le, Molecular diagnosis of COVID-19: challenges and research needs, *Anal. Chem.* 92 (2020) 10196–10209.
- [9] E. Valera, A. Jankelow, J. Lim, V. Kindratenko, A. Ganguli, K. White, J. Kumar, R. Bashir, COVID-19 point-of-care diagnostics: present and future, *ACS Nano* 15 (2021) 7899–7906.
- [10] G. Anderson, T. Esparza, B. Voelker, E. Hofmann, E. Goldman, Single-domain antibodies for the detection of SARS-CoV-2 nucleocapsid protein, *Anal. Chem.* 93 (2021) 7283–7291.
- [11] N. Sethuraman, S. Jeremiah, A. Ryo, Interpreting diagnostic tests for SARS-CoV-2, *JAMA* 323 (2020) 2249–2251.
- [12] B. Shang, X. Wang, J. Yuan, A. Vabret, X. Wu, R. Yang, L. Tian, Y. Ji, V. Deubel, B. Sun, Characterization and application of monoclonal antibodies against N protein of SRAS-coronavirus, *Biochem. Biophys. Res. Commun.* 336 (2005) 110–117.
- [13] L. Zhang, X. Fang, X. Liu, H. Ou, H. Zhang, J. Wang, Q. Li, H. Cheng, W. Zhang, Z. Luo, Discovery of sandwich type COVID-19 nucleocapsid protein DNA aptamers, *Chem. Commun.* 56 (2020) 10235–10238.
- [14] L. Hu, G. Xu, Applications and trends in electrochemiluminescence, *Chem. Soc. Rev.* 39 (2010) 3275–3304.
- [15] S. Cong, Z. Jiang, R. Zhang, H. Lv, J. Guo, L. Zhang, X. Lu, Polymer carbon nanodots: a novel electrochemiluminophore for dual mode detection of ferric ions, *Anal. Chem.* 94 (2022) 6695–6702.
- [16] Y. Wang, G. Zhao, H. Chi, S. Yang, Q. Niu, D. Wu, W. Cao, T. Li, H. Ma, Q. Wei, Self-luminescent lanthanide metal-organic frameworks as signal probes in electrochemiluminescence immunoassay, *J. Am. Chem. Soc.* 143 (2021) 504–512.
- [17] J. Li, M. Luo, H. Yang, C. Ma, R. Cai, W. Tan, Novel dual-signal electrochemiluminescence aptasensor involving the resonance energy transform system for kanamycin detection, *Anal. Chem.* 94 (2022) 6410–6416.
- [18] J. Li, M. Luo, C. Jin, P. Zhang, H. Yang, R. Cai, W. Tan, Plasmon-enhanced electrochemiluminescence of PTP-decorated Eu MOF-based Pt-tipped Au bimetallic nanorods for the lincomycin assay, *ACS Appl. Mater. Interfaces* 14 (2022) 383–389.
- [19] J. Ge, Y. Hu, R. Deng, Z. Li, K. Zhang, M. Shi, D. Yang, R. Cai, W. Tan, Highly sensitive microRNA detection by coupling nicking-enhanced rolling circle amplification with MoS₂ quantum dots, *Anal. Chem.* 92 (2020) 13588–13594.
- [20] C. Hong, X. Zhang, S. Ye, H. Yang, Z. Huang, D. Yang, R. Cai, W. Tan, Aptamer-pendant DNA tetrahedron nanostructure probe for ultrasensitive detection of tetracycline by coupling target-triggered rolling circle amplification, *ACS Appl. Mater. Interfaces* 13 (2021) 19695–19700.
- [21] M. Zhao, W. Zeng, Y. Chai, R. Yuan, Y. Zhuo, An affinity-enhanced DNA intercalator with intense ECL embedded in DNA hydrogel for biosensing applications, *Anal. Chem.* 92 (2020) 11044–11052.
- [22] W. Bai, A. Cui, M. Liu, X. Qiao, Y. Li, T. Wang, Signal-off electrogenerated chemiluminescence biosensing platform based on the quenching effect between ferrocene and Ru(bpy)₃²⁺-functionalized metal-organic frameworks for the detection of methylated RNA, *Anal. Chem.* 91 (2019) 11840–11847.
- [23] P. Li, L. Luo, D. Cheng, Y. Sun, Y. Zhang, M. Liu, S. Yao, Regulation of the structure of zirconium-based porphyrinic metal-organic framework as highly

- electrochemiluminescence sensing platform for thrombin, *Anal. Chem.* 94 (2022) 5707–5714.
- [24] W. Liu, A. Chen, S. Li, K. Peng, Y. Chai, R. Yuan, Perylene derivative/luminol nanocomposite as a strong electrochemiluminescence emitter for construction of an ultrasensitive microRNA biosensor, *Anal. Chem.* 91 (2019) 1516–1523.
- [25] J. Ye, L. Zhu, M. Yan, Q. Zhu, Q. Lu, J. Huang, H. Cui, X. Yang, Dual-wavelength ratiometric electrochemiluminescence immunosensor for cardiac troponin I detection, *Anal. Chem.* 91 (2019) 1524–1531.
- [26] Z. Wang, H. Guo, Z. Luo, Y. Duan, Y. Feng, Low-triggering-potential electrochemiluminescence from a luminol analogue functionalized semiconducting polymer dots for imaging detection of blood glucose, *Anal. Chem.* 94 (2022) 5615–5623.
- [27] H.J. Kim, K.S. Lee, Y.J. Jeon, I.S. Shin, J.I. Hong, Electrochemiluminescent chemodosimeter based on iridium(III) complex for point-of-care detection of homocysteine levels, *Biosens. Bioelectron.* 91 (2017) 497–503.
- [28] Y. Guo, J. Liu, Y. Chen, Y. Chai, Z. Li, R. Yuan, Boron and nitrogen-codoped carbon dots as highly efficient electrochemiluminescence emitters for ultrasensitive detection of hepatitis B virus DNA, *Anal. Chem.* 94 (2022) 7601–7608.
- [29] Y. Chen, Y. He, J. Zhao, J. Zhang, R. Yuan, S. Chen, Hydrophobic localized enrichment of co-reactants to enhance electrochemiluminescence of conjugated polymers for detecting SARS-CoV-2 nucleocapsid proteins, *Anal. Chem.* 94 (2022) 4446–4454.
- [30] J. Li, C. Wang, W. Wang, L. Zhao, H. Han, Dual-mode immunosensor for electrochemiluminescence resonance energy transfer and electrochemical detection of rabies virus glycoprotein based on Ru(bpy)₃²⁺-loaded dendritic mesoporous silica nanoparticles, *Anal. Chem.* 94 (2022) 7655–7664.
- [31] P. Zhang, Y. Zhang, X. Xiong, Y. Lu, N. Jia, A sensitive electrochemiluminescence immunoassay for glycosylated hemoglobin based on Ru(bpy)₃²⁺ encapsulated mesoporous polydopamine nanoparticles, *Sens. Actuators, B* 321 (2020) 128626–128635.
- [32] C. Hong, P. Zhang, K. Lu, Y. Ji, S. He, D. Liu, N. Jia, A dual-signal electrochemiluminescence immunosensor for high-sensitivity detection of acute myocardial infarction biomarker, *Biosens. Bioelectron.* 194 (2021) 113591–113598.
- [33] H. Xing, Q. Zhai, X. Zhang, J. Li, E. Wang, Boron nitride quantum dots as efficient coreactant for enhanced electrochemiluminescence of ruthenium(II) tris(2,2'-bipyridyl), *Anal. Chem.* 90 (2018) 2141–2147.
- [34] Y. Zhang, Z. Xu, Q. Wang, W. Hao, X. Zhai, X. Fei, X. Huang, Y. Bi, Unveiling the activity origin of ultrathin BiOCl nanosheets for photocatalytic CO₂ reduction, *Appl. Catal., B: Environmental* 299 (2021) 120679–120687.
- [35] C. Gong, J. Chu, S. Qian, C. Yin, X. Hu, H. Wang, Y. Wang, X. Ding, S. Jiang, A. Li, Y. Gong, X. Wang, C. Li, T. Zhai, J. Xiong, Large-scale ultrathin 2D wide-bandgap BiOBr nanoflakes for gate-controlled deep-ultraviolet phototransistors, *Adv. Mater.* 32 (2020) 1908242–1908251.
- [36] M. Guan, C. Xiao, J. Zhang, S. Fan, R. An, Q. Cheng, J. Xie, M. Zhou, B. Ye, Y. Xie, Vacancy associates promoting solar-driven photocatalytic activity of ultrathin bismuth oxychloride nanosheets, *J. Am. Chem. Soc.* 135 (2013) 10411–10417.
- [37] J. Cao, W. Cen, Y. Jing, Z. Du, W. Chu, J. Li, P-doped BiOCl for visible light photodegradation of tetracycline: an insight from experiment and calculation, *Chem. Eng. J.* 435 (2022) 134683–134694.
- [38] M. Naguib, M. Kurtoglu, V. Presser, J. Lu, J. Niu, M. Heon, L. Hultman, Y. Gogotsi, M.W. Barsoum, Two-dimensional nanocrystals produced by exfoliation of Ti₃AlC₂, *Adv. Mater.* 23 (2011) 4248–4253.
- [39] C. Liu, Y. Bai, W. Li, F. Yang, G. Zhang, H. Pang, In situ growth of three-dimensional MXene/metal-organic framework composites for high-performance supercapacitors, *Angew. Chem. Int. Ed.* 61 (2022) 202116282–202116287.
- [40] K. Nasrin, V. Sudharshan, K. Subramani, M. Sathish, Insights into 2D/2D MXene heterostructures for improved synergy in structure toward next-generation supercapacitors: a review, *Adv. Funct. Mater.* 32 (2022), 2110267–21102308.
- [41] H. Bao, Y. Qiu, X. Peng, J.A. Wang, Y. Mi, S. Zhao, X. Liu, Y. Liu, R. Cao, L. Zhuo, J. Ren, J. Sun, J. Luo, X. Sun, Isolated copper single sites for high-performance electroreduction of carbon monoxide to multicarbon products, *Nat. Commun.* 12 (2021) 238–246.
- [42] M. Javed, A. Mateen, S. Ali, X. Zhang, I. Hussain, M. Imran, S. Shah, W. Han, The emergence of 2D mxenes based Zn-ion batteries: recent development and prospects, *Small* (2022) 2201989–2202027.
- [43] Z. Ye, Y. Jiang, L. Li, F. Wu, R. Chen, Self-assembly of 0D-2D heterostructure electrocatalyst from MOF and MXene for boosted lithium polysulfide conversion reaction, *Adv. Mater.* 33 (2021) 2101204–2101214.
- [44] C. Zhang, L. Cui, S. Abdolhosseinzadeh, J. Heier, Two-dimensional MXenes for lithium-sulfur batteries, *Info 2* (2020) 613–638.
- [45] E. Aydin, J. El-Demellawi, E. Yarali, F. Aljamaan, S. Sansoni, A. Rehman, G. Harrison, J. Kang, A. El Labban, M. De Bastiani, A. Razaq, E. Van Kerschaver, T. Allen, O. Mohammed, T. Anthopoulos, H. Alshareef, S. De Wolf, Scaled deposition of Ti₃C₂T_x MXene on complex surfaces: application assessment as rear electrodes for silicon heterojunction solar cells, *ACS Nano* 16 (2022) 2419–2428.
- [46] X. Zha, X. Zhao, J. Pu, L. Tang, K. Ke, R. Bao, L. Bai, Z. Liu, M. Yang, W. Yang, Flexible anti-biofouling MXene/cellulose fibrous membrane for sustainable solar-driven water purification, *ACS Appl. Mater. Interfaces* 11 (2019) 36589–36597.
- [47] M. Faisal Shahzad, C. Hatter, B. Anasori, S. Hong, C. Koo, Y. Gogotsi, Electromagnetic interference shielding with 2D transition metal carbides (MXenes), *Science* 353 (2016) 1137–1140.
- [48] T. Laochai, J. Yukird, N. Promphet, J. Qin, O. Chailapakul, N. Rodthongkum, Non-invasive electrochemical immunosensor for sweat cortisol based on L-Cys/AuNPs/MXene modified thread electrode, *Biosens. Bioelectron.* 203 (2022) 114039–114048.
- [49] Q. Yu, C. Su, S. Bi, Y. Huang, J. Li, H. Shao, J. Jiang, N. Chen, Ti₃C₂T_x@nonwoven fabric composite: promising MXene-coated fabric for wearable piezoresistive pressure sensors, *ACS Appl. Mater. Interfaces* 14 (2022) 9632–9643.
- [50] W. Huang, Y. Wang, W. Liang, G. Hu, L. Yao, Y. Yang, K. Zhou, R. Yuan, D. Xiao, Two birds with one stone: surface functionalization and delamination of multilayered Ti₃C₂T_x MXene by grafting a ruthenium(II) complex to achieve conductivity-enhanced electrochemiluminescence, *Anal. Chem.* 93 (2021) 1834–1841.
- [51] L. Yang, T. Wu, Y. Du, N. Zhang, R. Feng, H. Ma, Q. Wei, Pegylation improved electrochemiluminescence supramolecular assembly of iridium(III) complexes in apoferritin for immunoassays using 2D/2D MXene/TiO₂ hybrids as signal amplifiers, *Anal. Chem.* 93 (2021) 16906–16914.
- [52] N. Qi Xun Xia, J. Yun, T. Zhang, S. Mane, K. Kim, Bismuth oxychloride/MXene symmetric supercapacitor with high volumetric energy density, *Electrochim. Acta* 271 (2018) 351–360.
- [53] Y. Wang, J. Sun, X. Qian, Y. Zhang, L. Yu, R. Niu, H. Zhao, J. Zhu, 2D/2D heterostructures of nickel molybdate and MXene with strong coupled synergistic effect towards enhanced supercapacitor performance, *J. Power Sources* 414 (2019) 540–546.
- [54] R. Zhao, C. Liu, X. Zhang, X. Zhu, P. Wei, L. Ji, Y. Guo, S. Gao, Y. Luo, Z. Wang, X. Sun, An ultrasensitive Ru₂P nanoparticles-reduced graphene oxide hybrid: an efficient electrocatalyst for NH₃ synthesis under ambient conditions, *J. Mater. Chem. A* 8 (2020) 77–81.